Atomic short-range order in SiGeSn alloys

Jifeng LIU

jifeng.liu@dartmouth.edu

Dartmouth College https://orcid.org/0000-0003-4379-2928

Shang Liu

Dartmouth College

Shunda Chen

George Washington University

Xiaochen Jin

George Washington University https://orcid.org/0000-0002-5391-6288

Jin-Hee Bae

Forschungszentrum Juelich

Ilias Bikmukhametov

University of Alabama

David Jaeger

University of North Texas

Omar Concepcion

Forschungszentrum Juelich

Alejandra Covian

Dartmouth College

Xiaoxin Wang

Dartmouth College

Cory Cline

Dartmouth College

Austin Akey

Harvard University

Lilian Vogl

University of California, Berkeley

Haochen Zhao

University of Delaware

Yuping Zeng

University of Delaware

Andrew Minor

University of California, Berkeley https://orcid.org/0000-0003-3606-8309

Shui-Qing Yu
University of Arkansas
Dan Buca
Forschungszentrum Jülich https://orcid.org/0000-0002-3692-5596
Tianshu Li
George Washington University https://orcid.org/0000-0002-0529-543X

Article

Keywords: : Short-range order, SiGeSn alloys, atom probe tomography, Poisson statistics, Machine-learning neuroevolution potentials

Posted Date: August 28th, 2024

DOI: https://doi.org/10.21203/rs.3.rs-4909892/v1

Additional Declarations: There is **NO** Competing Interest.

Atomic short-range order in SiGeSn alloys

Shang Liu[1†], Shunda Chen[2†], Xiaochen Jin[2], Jin-Hee Bae[3], Ilias Bikmukhametov[4], David Jaeger[5], Omar Concepcion[3], Alejandra Cuervo Covian[1], Xiaoxin Wang[1], Cory T. Cline[1], Austin Akey[6], Lilian M. Vogl[7], Haochen Zhao[8], Yuping Zeng[8], Andrew M. Minor[7], Shui-Qing Yu[9], Dan Buca[3], Tianshu Li[2], Jifeng Liu[1*]

[1]Thayer School of Engineering, Dartmouth College, 15 Thayer Drive, Hanover, 03755, NH, USA.
[2]Department of Civil and Environmental Engineering, George Washington University, Washington, 20052, DC, USA.
[3]Peter Gruenberg Institute 9 (PGI-9), Forschungszentrum Juelich, Juelich, 52428, Germany.
[4]Department of Metallurgical & Materials Engineering, University of Alabama, Tuscaloosa, 35405, AL, USA.
[5]Materials Research Facility, University of North Texas, Denton, 76201, TX, USA.
[6]Center for Nanoscale Systems, Harvard University, Cambridge, 02138, MA, USA.
[7]Department of Materials Science and Engineering, University of California, Berkeley, 94720, CA, USA.
[8]Department of Electrical and Computer Engineering, University of Delaware, Newark, 19716, DE, USA.
[9]Department of Electrical Engineering and Computer Science, University of Arkansas, Fayetteville, 72701, AR, USA.

*Corresponding author(s). E-mail(s): Jifeng.Liu@dartmouth.edu;
†These authors contributed equally to this work.

Abstract

Neighborhood at atomic scale is important for the properties of advanced alloys. The preference or avoidance between neighboring atomic species is known as

chemical short-range order (SRO). While SRO in metallic medium/high entropy alloys has garnered substantial attention recently, understanding SRO in semiconductor alloys remains underdeveloped. Motivated by theoretically predicted SRO and its dramatic impact on band structure, here we perform statistical analyses of atom probe tomography data to quantify SRO in $Si_xGe_{1-x-y}Sn_y$ alloys (x<12 at.%, y<16 at.%). Leveraging a side-by-side experiment-theory comparison at the same spatial scale enabled by machine-learning neuroevolution potentials of first-principles accuracy, we reveal, for the first time, a notable SRO favoring Si-Si 1^{st} nearest neighbors even at dilute Si and Sn compositions. The SRO can be tuned by varying precursors, offering a new degree of freedom for band engineering beyond composition and strain, and enabling new phase-change materials based on SRO transitions for Si electronics/photonics.

Keywords: Short-range order, SiGeSn alloys, atom probe tomography, Poisson statistics, Machine-learning neuroevolution potentials

1 Introduction

The importance of neighborhood has long been recognized in human civilization. For example, ancient China has a well-known story that Mencius, a famous philosopher in 300 B.C., moved 3 times with his widowed mom in his childhood to find a good neighborhood for proper education.[1] Interestingly, neighborhood at the atomic scale turns out to be equally important for the properties of advanced alloy materials. For a given atomic species in an alloy comprising several elements, it matters which species of atoms are their 1^{st}, 2^{nd} and 3^{rd} nearest neighbors or even at longer range. The preference or avoidance of certain atomic species in the K^{th} nearest neighbor (KNN) lattice sites is referred as chemical short-range order (SRO). This is in contrast to random alloys, where all atoms distribute randomly on the lattice sites without any preference of neighboring atomic species. In recent years, chemical SRO in metallic medium and high entropy alloys (MEA and HEA) has received substantial attention as it can profoundly impact their mechanical and electrical properties.[2–8] Since an MEA/HEA requires more than 3/5 principal components,[9, 10] the SRO in these cases occurs in more or less equimolar alloys rather than dilute alloys. The corresponding SRO domains also have well-defined long-range ordered (LRO) counterparts such as $D0_3$ or B_2,[7] therefore named after the corresponding LRO.

By comparison, SRO in dilute metallic alloys with a few percent of solute atoms is less commonly studied either theoretically [11] or experimentally.[12–15] This is because usually the low concentration of solute atoms limits their interactions, making it difficult for them to exhibit significant chemical ordering. Furthermore, SRO in semiconductor alloys is rarely studied compared to their metallic counterparts, even though different types of LRO such as CuPt-A, CuPt-B, and CuAu-I etc. have been observed in equimolar ternary III-V compounds.[16] While SRO in dilute nitride semiconductors was theoretically predicted previously, it was mostly disapproved by experimental results.[17] Therefore, investigating SRO in semiconductor alloys, especially dilute

semiconductor alloys, could potentially reveal new physics in atomic ordering for novel device applications.

As a representative semiconductor alloy, SiGeSn have received significant interest for short-wave and mid-infrared (SWIR and MIR) optoelectronics applications as Si-compatible Group IV semiconductors. The latest advancements in Si-based GeSn/Ge photodetectors,[18–24] GeSn/SiGeSn hetero-structures [25–29] and quantum well (QW) lasers [30–33] demonstrated the potential of SiGeSn alloys for integrated photonics on Si.[34–37] However, unlike III-V and II-VI semiconductors, the lattice-matched hetero-junction is still missing in SiGeSn devices due to the limited choices in lattice constant-bandgap space. For example, theories showed that lattice-matched type-I confinement between $Ge_{0.9}Sn_{0.1}$ and SiGeSn only provides an energy barrier lower than 0.1 eV for both the conduction and valance bands.[38] A desirably higher band offset is important to reach room temperature lasing,[25] but it requires a larger difference in Si composition between the QW and the barrier thus a larger lattice mismatch, which brings a key issue for epitaxial growth. Inspiringly, very recent studies predicted the existence of SRO in GeSn and SiGeSn alloys and illustrated the dramatic impact of SRO on their band structures.[39–42] For example, theoretical models show that the band gap in $Si_{0.125}Ge_{0.625}Sn_{0.25}$ increases from ∼0.25 eV (direct) for a random alloy to ∼0.75 eV (indirect) for an alloy with enhanced SRO.[39] These new findings give rise to an alternative and highly effective direction towards perfectly lattice-matched iso-composition hetero-junctions and QWs with large band offsets by engineering SRO.[43] Moreover, first-principles calculations also show SRO has a strong impact on the thermal conductivity of SiGeSn alloys,[44] forecasting the possibility to use SiGeSn as the first CMOS compatible thermoelectric material for on-chip energy harvesting.[45, 46]

However, experimentally quantifying the extent of SRO still remains a big challenge,[2–8], especially underdeveloped for semiconductor alloys. While four dimensional scanning transmission electron microscopy (4D-STEM) has been applied to study and map SRO domains at nm-scale in medium and high entropy alloys,[2–4, 47, 48], it is usually difficult to directly correlate the 4D-STEM results to the atomic species that exhibit SRO and multiple sources have been shown to potentially contribute to the diffraction signals.[49, 50] Extended X-ray absorption fine structure (EXAFS) was first carried out by Shimura et al. to extract SRO information in SiGeSn alloys,[51] but the result reflects an averaged SRO over a large volume (∼100 um^2 area × ∼1 um thickness) while theory predicted that the statistical spatial distribution of SRO at nanoscale is also important.[39, 41, 42] Mukherjee et al. later employed atom probe tomography (APT) to analyze the radial distribution function (RDF) of Si, Ge and Sn elements and observed a repulsive interaction between Sn and Si.[52] However, their RDF is meaningful only for $r \geq 0.5$ nm which is beyond 3NN, while theories predict it is 1NN-3NN that exhibit the most significant SRO with the largest impact on the band structure.[39–42] Ideally, local ordering in 1NN-3NN can be readily examined once atomic positions and species are identified by APT, as shown in studies for metals.[53–56] However, it is challenging to directly derive accurate RDF and SRO of semiconductors from APT because the large spatial error induced by

the non-uniform electric field during the field evaporation of semiconductors, or the so-called local magnification issue.[57–59]

Here, we apply physics-informed statistical analyses [60] to the APT measurements of $Si_xGe_{1-x-y}Sn_y$ (x < 12 at.%, y < 16 at.%) alloys and leverage side-by-side experiment-theory comparison based on first-principles neuroevolution potentials to reveal a distinct and notable preference for Si-Si 1NN in SiGeSn alloys grown by chemical vapor deposition (CVD). This trend holds even for dilute SiGeSn alloys with a few percent of Si and Sn, driven by the minimization of local distortion in this atomic size mismatched system against phase separation. To our knowledge, this is the first experimental evidence showing not only Si-Si SRO in SiGeSn alloys but also notable SRO in any dilute semiconductor alloy system, without any LRO counterparts at all, in sharp contrast to SRO in more or less equimolar MEA/HEAs with clear LRO counterparts. The experimental results are consistent not only with theoretical modeling but also 4D-STEM analyses in reciprocal space that will be published separately.[61, 62] Our research also suggests that Si-Si SRO in SiGeSn thin films could potentially be modified by Si precursors, revealing an exciting new approach to tailor the band structure of SiGeSn alloys towards lattice-matched heterostructures and QWs. Furthermore, this first experimental discovery of notable SRO in dilute semiconductor alloys with large atomic size mismatch enriches our fundamental understanding of phase stability in terms of random to SRO transitions, one of the central themes of materials science. Potential transitions from random to SRO alloys and vice versa by swapping neighboring atoms may open a door towards novel phase-change electronic/photonic devices on Si based on SRO rather than LRO transitions in existing systems, which can potentially boost the speed and energy efficiency of the phase transition process for functional materials.

2 Results and discussion

2.1 SiGeSn samples and SRO

A set of 14 SiGeSn samples grown by CVD are investigated. The Si precursor for samples A1-A4, B1-B4, C1-C6 was SiH_2Cl_2, Si_2H_6,and SiH_4, respectively. Si composition ranges from 1.2 to 11.3 at.% while Sn composition varies from 2.5 to 15.9 at.%. More details about atomic composition will be presented later. The SRO is derived from APT data using the physics-informed Poisson-KNN statistical method developed in Ref.[60]. Through a statistically weighted summation of nominal KNN in APT data, the true KNN shells are reconstructed, enabling the calculation of the probability of an A atom having a B atom in its true KNN shell, i.e., P_{A-B}^{KNN} (A, B = Si, Ge, Sn). The SRO parameter is then derived as the ratio of P_{A-B}^{KNN} to the atomic percentage of B in the region x_B:

$$\alpha_{A-B}^{KNN} = \frac{P_{A-B}^{KNN}}{x_B} \tag{1}$$

Specifically, $\alpha_{Si-Si}^{1NN} > 1$ indicates a tendency of Si-Si clustering, while $\alpha_{Si-Si}^{1NN} < 1$ indicates a tendency of Si-Si de-clustering. Also note that our definition of SRO parameter in Equation (1) is exactly equal to 1 minus the Warren-Cowley SRO parameter commonly used in theoretical literature. This experimental definition in Equation (1) is

preferred because it more intuitively corresponds a larger SRO parameter to the preference of A-B neighbors. SRO is analyzed within 10 nm × 10 nm × 10 nm nanocubes in each sample (except samples B3 and B4), and 3D SRO maps are generated accordingly. Each nanocube contains more than 10000 atoms, providing sufficient data for statistical analysis. SRO in samples B3 and B4 is calculated in 10 nm × 10 nm × 5 nm nanocubes (∼7000 atoms) because the thickness of SiGeSn barriers in the QW structures is smaller than 10 nm.

2.2 Impact of APT laser pulse energy on SRO analyses

The APT data collected from different institutions were measured under varying conditions, particularly with respect to the pulsed laser energy. To rule out the impact of laser energy on the SRO parameters, we first compared the SRO in the same sample (A1) measured at different laser energies using the same APT equipment at Oak Ridge National Lab, as listed in Table 1. Laser mode with 60, 20, 10 pJ/pulse laser energy was used to evaporate atoms from sample A1 for APT data. Voltage mode (i.e., using electric field only without laser evaporation) was also used for a comparison (the last row in Table 1). SRO parameters were analyzed in ∼20-50 nanocubes, each with dimensions of 10 nm × 10 nm × 10 nm, for each condition. The mean SRO value was then compared with an error range calculated using the the standard error of mean (SEM). The SEM is defined as the standard deviation (SD) divided by the square root of the number of the nanocubes (N), i.e., $SEM = SD/\sqrt{N}$. By considering the number of nanocubes, the SEM accurately reflects the true error of the mean. It is found that Si-Si 1NN SRO α^{1NN}_{Si-Si} is almost identical in these cases and it is not affected by pulsed laser energy ranging from 0 to 60 pJ. In particular, the Si-Si 1NN SRO parameters are practically the same for 0 vs. 60 pJ. Note that higher pulsed laser energy results in stronger thermal evaporation vs. field evaporation, which can perturb the atomic positions via thermal excitation. On the other hand, it can reduce the DC voltage required to evaporate the atoms, which helps avoid sample fracture, especially in brittle materials such as semiconductors. Increasing laser pulse energy also leads to a larger ratio of 1+ ions to 2+ ions for Si, Ge and Sn, which serves as a good indicator of thermal perturbation when comparing APT data acquired by different equipment under different conditions. Results in Table 1 suggests Si-Si 1NN SRO is not impacted by pulsed laser energy when the Si+/Si++ ratio is in the range of 0-2.5 and the Ge+/Ge++ ratio is within 0-4.0. Therefore, all the APT data selected in this paper were acquired by 0-60 pJ/pulse with the 1+/2+ ion ratios around the ranges specified above in order to avoid any artifacts due to different measurement conditions.

Another important piece of information from Table 1 is that, under the same laser pulse energy or thermal perturbation, Sn shows much smaller 1+/2+ ion ratio than Si and Ge. At laser pulse energy below 20 pJ, Sn atoms are almost entirely field-evaporated as indicated by the predominance of 2+ ions. Since Sn atoms are well known to migrate under a large electric field,[63, 64] this factor could reduce the accuracy of quantitative Sn-Sn SRO analyses compared to Si-Si. This will be discussed later.

Table 1 SRO of SiGeSn sample A1 versus laser energy

Sample #	Si at.%	Ge at.%	Sn at.%	Laser energy (pJ)	Si+/ Si++	Ge+/ Ge++	Sn+/ Sn++	**Mean α^{1NN}_{Si-Si}**	# of nanocubes
A1	4.5	89.0	6.5	60	2.44	3.97	1.05	**1.03±0.03**	20
				20	0.30	0.17	0.01	**1.05±0.03**	47
				10	0.13	0.05	0.00	**1.04±0.03**	36
				0	0.00	0.00	0.00	**1.02±0.02**	45

2.3 SRO in SiGeSn

Fourteen different SiGeSn samples grown by 3 types of CVD precursors were analyzed. Their composition and SRO are summarized in Table 2. Again, the SRO is represented as the mean value ± SEM. As a representative example, Fig. 1 shows APT and STEM data of sample A1 grown by SiH_2Cl_2. As shown in Fig. 1a, SiGeSn sample A1 is the barrier in a SiGeSn/GeSn/SiGeSn multiple quantum well (MQW) structure.[30] Fig. 1b shows the composition profile. The SiGeSn region we investigated has 4.5 at.% Si and 6.5 at.% Sn on average. 3D SRO mapping is exemplified in Fig. 1c. α^{1NN}_{Si-Si} is 1.04 ± 0.01 over 148 10 nm × 10 nm × 10 nm nanocubes in 4 tips. The high-resolution STEM (HRSTEM) image and Energy Dispersive X-Ray Spectroscopy (EDS) mapping of sample A1 are shown in Fig. 1d, indicating no defects near the interface between SiGeSn and GeSn.

Table 2 Composition and SRO of 14 SiGeSn samples

Si Precursor	Sample #	Si at.%	Ge at.%	Sn at.%	Si:Sn ratio	**Mean α^{1NN}_{Si-Si}**	Mean α^{1NN}_{Sn-Sn}	# of nanocubes
SiH_2Cl_2	A1	4.5	89.0	6.5	0.69	**1.04±0.01**	1.01±0.01	148
	A2	6.6	85.8	7.6	0.87	**1.03±0.01**	1.00±0.01	179
	A3	3.7	88.3	8.0	0.46	**1.09±0.01**	0.99±0.01	81
	A4	1.2	88.6	10.2	0.12	**1.15±0.05**	1.01±0.00	81
Si_2H_6	B1	4.5	83.1	12.4	0.36	**1.03±0.01**	1.00±0.00	100
	B2	2.1	82.0	15.9	0.13	**0.98±0.13**	1.01±0.01	9
	B3	10.8	78.5	10.7	1.01	**1.08±0.01**	1.01±0.01	64
	B4	4.2	81.4	14.4	0.29	**1.06±0.03**	0.99±0.01	64
SiH_4	C1	1.3	93.3	5.5	0.24	**1.11±0.05**	1.01±0.01	36
	C2	3.2	92.8	4.0	0.80	**1.06±0.01**	1.02±0.01	79
	C3	1.7	92.8	5.6	0.30	**1.11±0.02**	1.00±0.01	63
	C4	11.3	86.2	2.5	4.52	**1.02±0.01**	1.05±0.06	30
	C5	4.1	92.7	3.2	1.28	**1.07±0.03**	0.98±0.03	36
	C6	2.4	93.6	4.0	0.60	**1.00±0.04**	1.00±0.02	72

Similarly, APT data of sample B1 (grown by Si_2H_6 precursor) and C1 (grown by SiH_4 precursor) are shown in Fig. 2. Sample B1 is also a MQW sample, as shown in Fig. 2a and b. The SiGeSn barrier has 4.5 at.% Si and 12.4 at.% Sn. The SRO mapping in sample B1 is shown in Fig. 2c, with a similar level of fluctuation as sample A1. Sample C1 is a SiGeSn thin film grown on Ge, with 1.3 at.% Si and 5.5 at.% Sn, as shown in Fig. 2d and e. Compared to the SRO in sample A1 and B1, the α^{1NN}_{Si-Si} in sample C1 (1.11 ± 0.05) has a larger mean and fluctuation, as illustrated by more dark

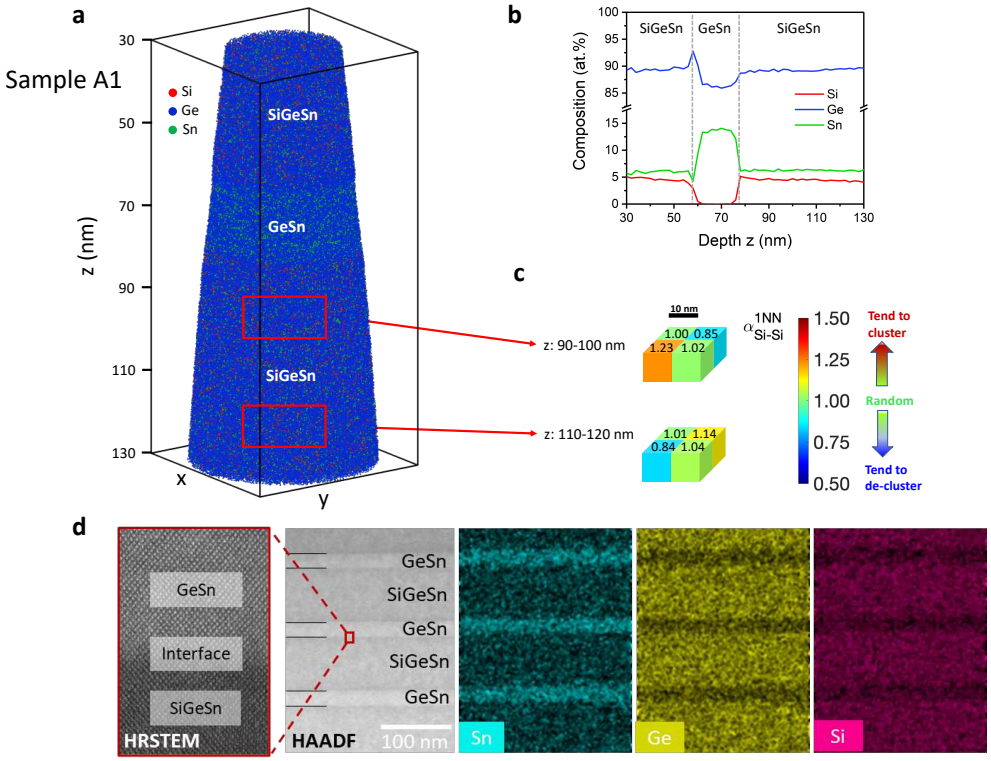

Fig. 1 APT and STEM data of sample A1 grown by SiH_2Cl_2. SiGeSn is the barrier in a SiGeSn/GeSn/SiGeSn quantum well (QW) structure. a) Reconstructed APT data. b) Composition profile. c) 3D SRO mapping examples in SiGeSn region. d) HRSTEM and EDS mapping of the sample.

red (∼1.5) regions in Fig. 2f. Please note that the relatively larger α^{1NN}_{Si-Si} in sample C1 compared to sample A1 and B1 does not result from C1 being a SiGeSn thin film on Ge. In fact, samples C2-C6 are also SiGeSn thin films on Ge, yet C4 and C6 have a smaller α^{1NN}_{Si-Si}. The large α^{1NN}_{Si-Si} in C1 and C3 is most likely due to the small Si:Sn ratio, as will discussed in the trend shown in Fig. 3a.

As summarized in Table 2 and Fig. 3a, the preference of Si-Si 1NN is observed in almost all SiGeSn samples except B2 and C4, with an average α^{1NN}_{Si-Si} ranging from 0.98 to 1.15. These include notable Si-Si 1NN SRO in dilute SiGeSn alloys such as A3-A4, C1-C3, and C5. To the best of our knowledge, this is the first experimental demonstration of notable SRO in dilute semiconductor alloys. This result largely agrees with the theoretical prediction based on SiGeSn supercells of the similar compositions, generated through large-scale Monte Carlo sampling based on our developed machine-learning neuroevolution potential for SiGeSn alloys, shown in Fig. 3a, with a clear preference of Si-Si 1NN and α^{1NN}_{Si-Si} ranging from 1.2 to 1.3. The degree of preference for Si-Si 1NN pairs from the APT data is smaller than the predictions due to the perturbation of atom positions in APT measurements, which leads to the assignment

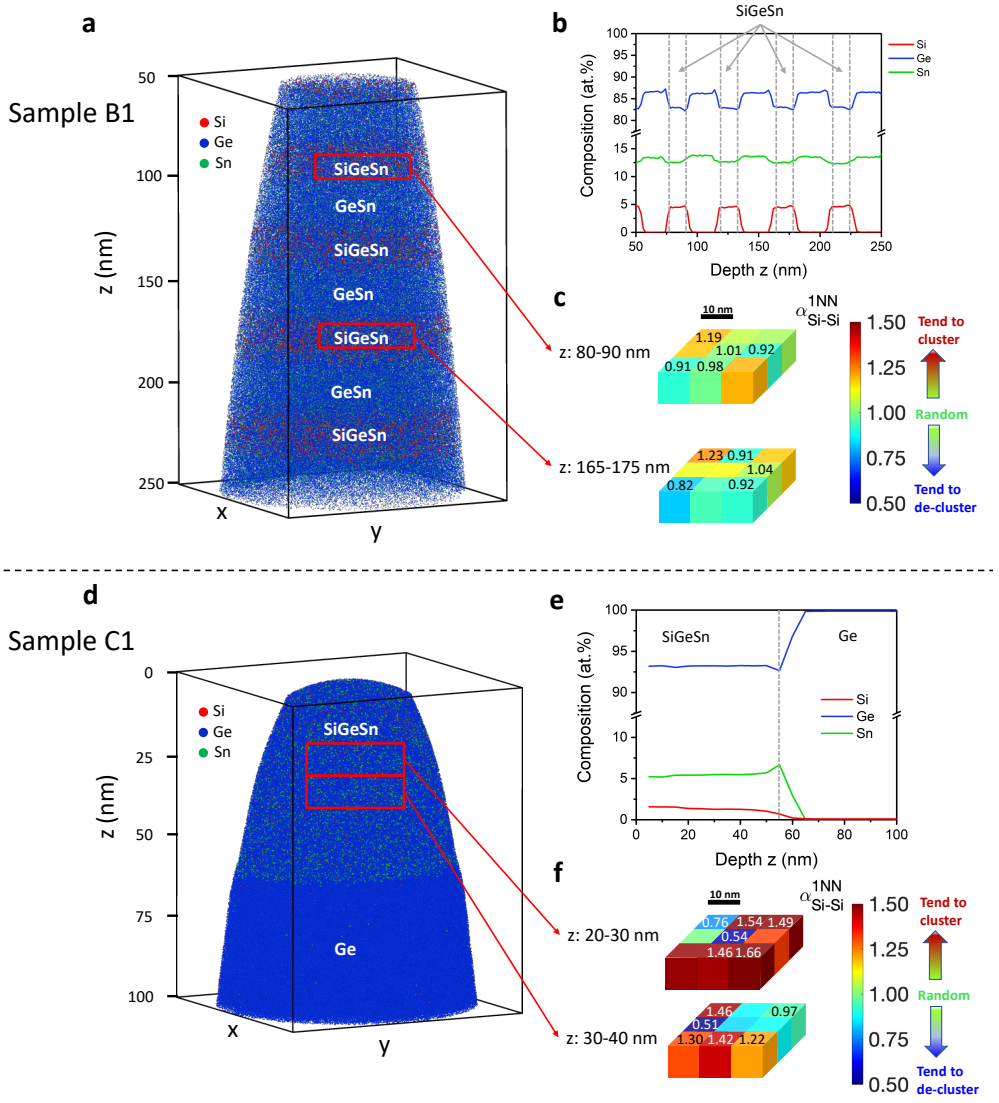

Fig. 2 APT data of sample B1 (grown by Si_2H_6) and C1 (grown by SiH_4). a) Reconstructed APT data in B1. b) Composition profile in B1. c) 3D SRO mapping examples in B1. d) Reconstructed APT data in C1. e) Composition profile in C1. f) 3D SRO mapping examples in C1.

of some Si-Si 1NN pairs to the 2NN and 3NN shells (Fig. 3b) and dilutes the Si-Si 1NN SRO parameters. More discussions will be provided later.

In contrast to α^{1NN}_{Si-Si} that are predominantly greater than 1, the average Sn-Sn SRO α^{1NN}_{Sn-Sn} is almost identical to 1 (except C4), meaning Sn-Sn 1NN pairs are less likely to occur than Si-Si 1NN in most of the SiGeSn samples. We also noted that the Sn-Sn 1NN SRO parameters in SiGeSn are slightly lower than their GeSn

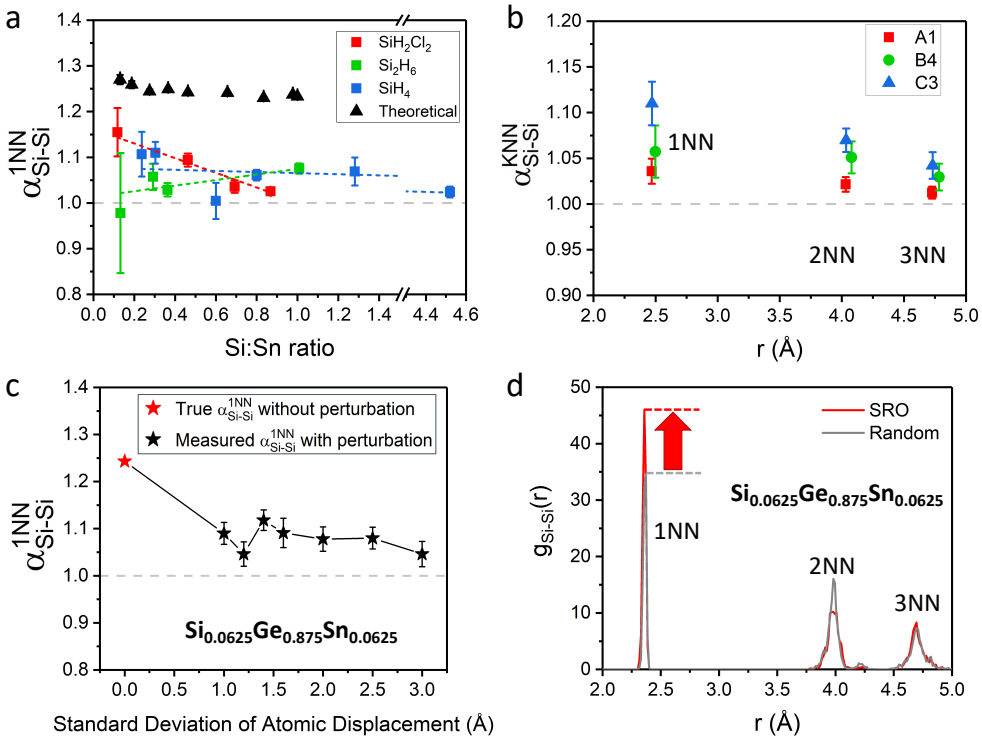

Fig. 3 a) Si-Si 1NN SRO in SiGeSn versus ratio between Si and Sn composition. The error bars are the standard error of mean (SEM). The black triangles represent the theoretical prediction, enabled by first-principles machine-learning neuroevolution potential, using supercells of the same size as those in experiment, with SEM obtained by averaging 900 configurations for each composition. The red, green and blue squares represent experimental data measured in SiGeSn grown by precursors SiH_2Cl_2, Si_2H_6 and SiH_4, respectively. The corresponding dashed lines are the linear fits of the data from each of the three precursors. b) Si-Si 1NN-3NN SRO in sample A1, B4 and C3. The error bars are SEM. c) Measured SRO from theoretically simulated $Si_{0.0625}Ge_{0.875}Sn_{0.0625}$ supercells as a function of atomic position perturbation. The red star is the true α^{1NN}_{Si-Si} without perturbation. The black stars are the measured average α^{1NN}_{Si-Si} as a function of the magnitude of perturbation, quantified by standard deviation of atomic displacement. The error bars represent the SEM of α^{1NN}_{Si-Si} over 10 different configurations. d) Si-Si RDF in theoretically simulated $Si_{0.0625}Ge_{0.875}Sn_{0.0625}$ supercells.

counterparts,[60, 65] which is also qualitatively consistent with the theoretical prediction, as will be detailed in the next section. On the other hand, although Sn-Sn repulsion is predicted in SiGeSn,[39] it is not quantitatively observed in the APT data. This is because the Sn-Sn 1NN SRO parameter from APT analyses is more susceptible to atomic position perturbation in the APT measurements due to the compensation between 1NN and 3NN shells, as will be detailed in the next section. Another factor is the surface migration of Sn atoms under a large electric field, as discussed earlier. Therefore, while we find that the relative comparison of Sn-Sn SRO parameters still holds true when atomic perturbation is smaller than 2.5 Å, as shown in Supporting

Information Fig. S1, Sn atoms may experience a larger perturbation in atomic positions than Si during APT measurements, leading to a lower accuracy in quantifying Sn-Sn SRO using APT.

The ratio between Si and Sn is also presented in Table 2 because theoretical prediction shows a dependence of Si-Si SRO on this ratio, as shown in Fig. 3a. The black triangles are theoretical α_{Si-Si}^{1NN} calculated based on 10.2 nm × 10.2 nm × 10.2 nm supercells generated using Monte Carlo (MC)/machine-learning neuroevolution potentials (NEP) method (see methods for details). The error bars represent the SEM obtained from 900 different supercells evenly selected from MC/NEP trajectories ranging from 100 000th to 1 000 000th MC step, with a spacing of 1000 step, for each composition. According to the simulations, a relatively stronger Si-Si 1NN preference is observed when Si:Sn ratio becomes smaller. This supports the idea that SRO exists to minimize the distortion (or strain) created by the substitution of Si and Sn in the Ge lattice.[41] Given that Sn atoms are 15% larger than Ge atoms while Si atoms are about 4% smaller, a certain degree of preference for Si-Si 1NN could effectively counteract the lattice dilation induced by nearby Sn atoms, e.g. through a Si-Si-Sn nearest neighboring configuration to reduce the local strain. The more the Sn or the fewer the Si atomic percentage in Ge, the more pronounced the dilational lattice distortion, which requires more Si-Si 1NN to compensate the distortion through Si-Si-Sn neighboring configurations. This theoretically predicted trend is indeed largely consistent with the trends in the SiGeSn samples grown by SiH_2Cl_2 and SiH_4 precursors (see the red and blue squares in Fig. 3). The impact of CVD precursors will be further discussed in a later section.

To better understand the underestimated Si-Si 1NN SRO parameters in the experimental data compared to theoretical predictions, as briefly mentioned earlier, Si-Si 2NN and 3NN SRO parameters of sample A1, B4 and C3 are shown in Fig. 3b. Here we select one sample for each precursor. Clearly, the average α_{Si-Si}^{2NN} and α_{Si-Si}^{3NN} are also slightly larger than 1 in these samples due to the atomic position perturbation that leads to the assignment of some true Si-Si 1NN pairs to the 2NN or 3NN shells. This will be detailed next.

2.4 Impact of atomic position perturbation on APT SRO analyses

To further confirm the impact of atomic position perturbation in APT data on Si-Si SRO parameters retrieved by Poisson-KNN method, we generated SRO structural models (10.2 nm × 10.2 nm × 10.2 nm, 46656 atoms) of $Si_{0.0625}Ge_{0.875}Sn_{0.0625}$ by employing Monte Carlo (MC) sampling using a machine-learning neuroevolution potential for Si-Ge-Sn alloys we developed herein (see methods), as an extension of our recently developed neuroevolution potential for GeSn alloys.[42] The MC/NEP sampling yields a Si-Si 1NN SRO parameter $\alpha_{Si-Si}^{1NN} = 1.24$. To mimic the limited detection efficiency in APT, we created ten distinct configurations by randomly removing 50% of the atoms within each configuration. Atomic positions were then spatially perturbed according to a Gaussian distribution [66] with a standard deviation of 1-3 Å to simulate the uncertainty in determining atomic positions in APT. Applying Poisson-KNN method to these perturbed structural models, we found the approach

yields an average Si-Si 1NN SRO parameter around 1.1 in $Si_{0.0625}Ge_{0.875}Sn_{0.0625}$ when the perturbation is within 1-3 Å. This degree of underestimation of α^{1NN}_{Si-Si} is almost identical to the difference between the theoretically predicted and experimentally measured α^{1NN}_{Si-Si} shown in Fig. 3a, suggesting that the perturbation in APT measurement can be the main reason that the measured α^{1NN}_{Si-Si} is lower than the predicted value. Furthermore, as shown in in Fig. 3d, the Si-Si radial distribution function (RDF) in the theoretical supercell (red curve) exhibits a notably higher 1NN peak but only a slightly lower 2NN peak compared to that in a random alloy (grey curve), with the 3NN peaks being nearly identical in both cases. This indicates that the intermixing of 1NN with 2NN or 3NN, induced by perturbations in APT measurements, will dilute the measured Si-Si 1NN SRO α^{1NN}_{Si-Si} while increasing Si-Si 2NN and 3NN SRO parameters close to or above those of the random alloys. It also explains the trend observed in Fig. 3c, where the measured α^{1NN}_{Si-Si} gradually decreases as perturbation increases. Consequently, the measured α^{2NN}_{Si-Si} and α^{3NN}_{Si-Si} become larger than 1 due to this intermixing, as confirmed by the APT experimental results in Fig. 3b.

As alluded earlier, we also checked the impact of perturbation on measured Sn-Sn SRO using theoretically simulated models, as shown in Supporting Information Fig. S1a, despite that the predicted Sn-Sn repulsion is not observed in APT. The measured α^{1NN}_{Sn-Sn} is more sensitive to the perturbation than α^{1NN}_{Si-Si}. This is because the Sn-Sn RDF in SRO SiGeSn alloys shows strong depletion of 1NN and strong enhancement of 3NN that compensate each other upon perturbation (see Sn-Sn RDF in Supporting Information Fig. S1b), while Si-Si RDF is dominated by 1NN enhancement without strong depletion from either 2NN or 3NN. Consequently, the intermixing of Sn-Sn 1NN and 3NN due to atomic position perturbation in the APT data will significantly compensate the SRO of each other towards a random alloy and smears out the measured Sn-Sn 1NN SRO (see Fig. S1c in the Supporting Information). In contrast, the Si-Si 1NN SRO parameter only gets diluted, while overall Si-Si 1NN-3NN all show enhancement even upon atomic site perturbation, as discussed previously in Fig. 3b.

2.5 Precursor effect

As mentioned earlier, while the SiGeSn samples grown by SiH_2Cl_2 and SiH_4 (red and blue squares and linear fitting dashed lines in Fig. 3a) largely follow the theoretical trend that the Si-Si 1NN SRO increases as the Si:Sn ratio decreases, the samples grown by Si_2H_6 (green squares and linear fitting dashed line in Fig. 3a) appear to follow the opposite trend. To directly assess the influence of Si precursors on SRO, we selected sample B4 and C3 for comparison. The former is grown by Si_2H_6 while the latter is grown by SiH_4. These two samples have a similar Si-to-Sn ratio (∼0.3) and a comparable ion-charge ratio (∼2.1 for Si+/Si++ and ∼2.8 for Ge+/Ge++), allowing us to mitigate the influence of temperature and perturbation. Histograms of Si-Si and Sn-Sn 1NN SRO statistical distribution is shown in Fig. 4. α^{1NN}_{Si-Si} is relatively smaller in the sample grown by Si_2H_6 (1.06) than the sample grown by SiH_4 (1.11), but Sn-Sn SRO parameter α^{1NN}_{Sn-Sn} is almost the same for these two samples (∼1.00). This comparison, together with the clearly different trends in Si-Si 1NN SRO vs. Si:Sn ratio for Si_2H_6, SiH_2Cl_2 and SiH_4, (Fig. 3a), suggests that Si-Si SRO could be potentially tuned by choosing different Si precursors. Based on

this finding, we expect that changing the Sn precursor from $SnCl_4$ to others such as SnD_4 may also produce different Sn-Sn SRO. A likely reason for the precursor effect is the surface chemistry and surface termination, which could impact the SRO on the growth front. Additionally, the growth rate using Si_2H_6 precursor is higher compared to SiH_4,[67] meaning the growth process with Si_2H_6 might be further from thermodynamic equilibrium. As a result, the SRO does not align with the theoretical value predicted at thermodynamic equilibrium. We will investigate more about the control of SRO through CVD precursors in the future.

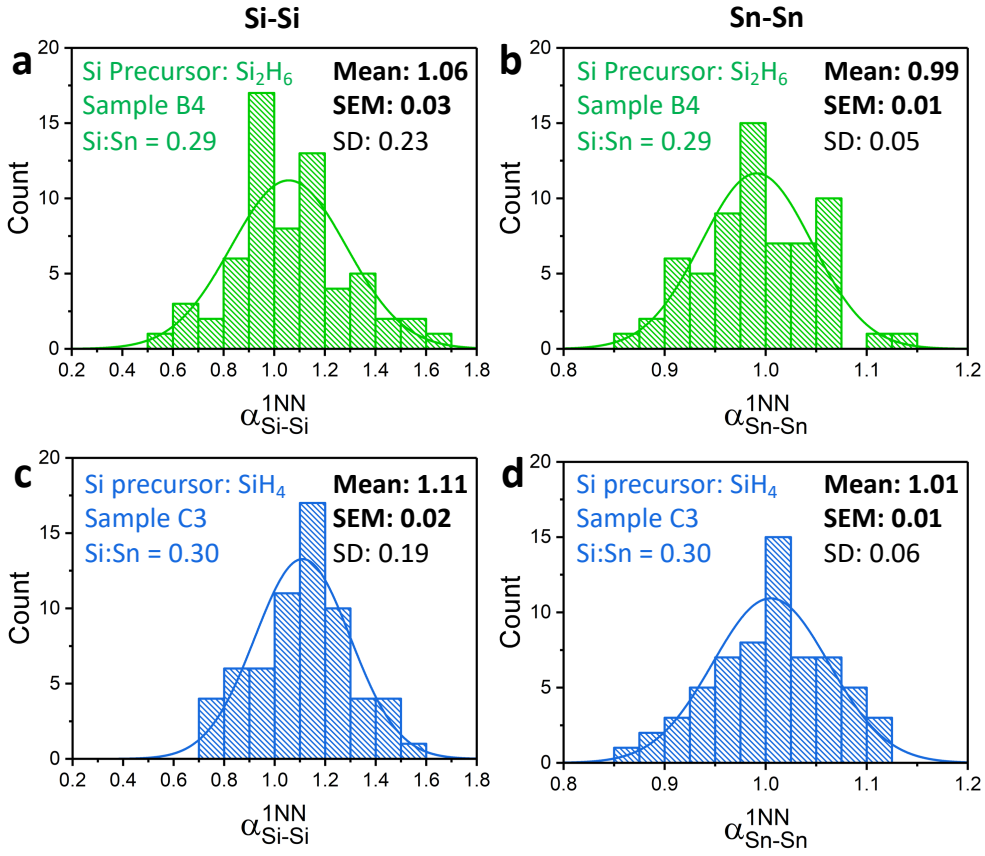

Fig. 4 Histogram of Si-Si and Sn-Sn 1NN SRO in sample B4 and C3. a), b) α^{1NN}_{Si-Si} and α^{1NN}_{Sn-Sn} in sample B4. Sample size n = 64 (nanocubes). c), d) α^{1NN}_{Si-Si} and α^{1NN}_{Sn-Sn} in sample C3. Sample size n = 63 (nanocubes).

2.6 Band structure of random vs. SRO dilute SiGeSn alloys

To investigate the impact of SRO on the band structure in dilute SiGeSn alloys, the theoretical band structure of $Si_{0.0625}Ge_{0.875}Sn_{0.0625}$ (with a SRO discussed in Fig.

3c,d) is computed and shown in Fig. 5, compared with the random alloy with the same composition. The predicted band gap is listed in Table 3. It is found that even with this low Sn and Si composition (6.25% for both), SRO already increases the direct bandgap by ∼60 meV, i.e., 10 %. As the electrical pumped GeSn/SiGeSn QW laser works at 100-150 K to date [25–27], increasing the QW depth by using a larger bandgap SRO SiGeSn barrier without increasing the lattice mismatch would help with carrier confinement towards a room temperature laser. On the other hand, random SiGeSn alloys are more direct in band structure, thereby more suited for the QW region. As discussed earlier, switching CVD precursors could potentially offer such SRO control to optimize the QW structures. It is also worth noting that the fact that SRO slows down the indirect-to-direct gap transition in GeSn and SiGeSn system is fundamentally attributed to the preservation of local tetrahedrality of Ge atoms. In this regard, the transformation of Ge to direct gap semiconductor, either by tensile strain or Sn alloying, is essentially due to lattice distortion (either locally by Sn alloy or homogeneously by biaxial tensile strain), associated with the breaking of local perfect tetrahedrality (sp^3 hybridization). SRO will reduce this effect induced by Sn since it tends to minimize the elastic strain energy.

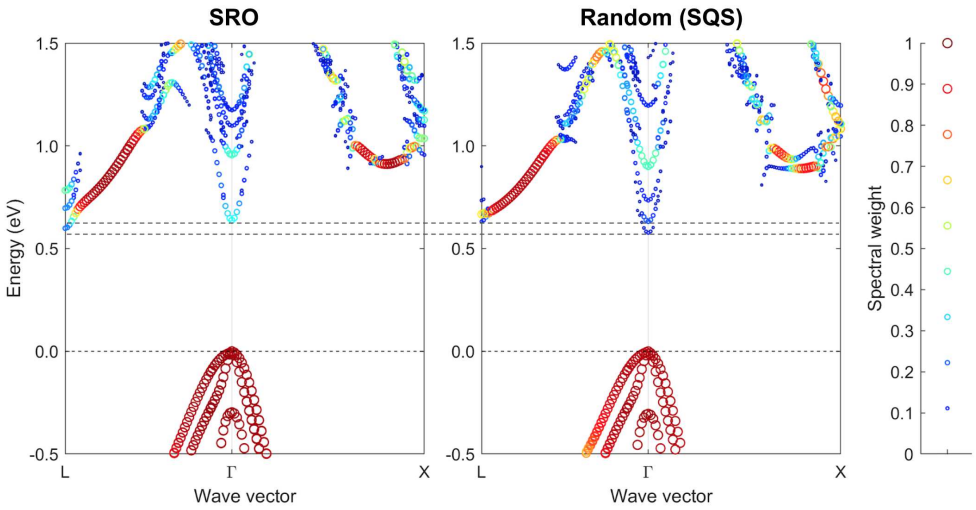

Fig. 5 Unfolded electronic band structure of $Si_{0.0625}Ge_{0.875}Sn_{0.0625}$ alloys with and without SRO. The direct band gap of the SRO alloy is about 0.1 eV larger than that of the random (SQS) alloy. The corresponding Bloch spectral weight, which quantifies the amount of Bloch character preserved in the supercell eigenvalue and how closely an electronic state resembles an ideal Bloch state in a perfect crystal, is color-coded and size-coded in the plot on the right. Larger sizes indicate states that closely match the ideal Bloch states, while smaller sizes indicate states that are more disordered or less Bloch-like.

Table 3 Predicted band gap of $Si_{0.0625}Ge_{0.875}Sn_{0.0625}$

	Δ_Γ (eV)	Δ_L (eV)
SRO	0.640	0.599
Random	0.577	0.632

2.7 Discussion

Our studies of SRO in SiGeSn alloys represent the first observation of notable SRO in dilute semiconductor alloys due to large atomic size differences. Si-Si 1NN becomes preferred in order to compensate for the local lattice dilation induced by the large Sn atoms, even for dilute solute concentrations. The 15% atomic size mismatch between Sn and Ge sits right at the border of Hume-Ruthery rules, while the mismatch between Si and Sn is even larger. Usually, such atomic size mismatch would lead to either phase separation or compound formation. In SiGeSn system, we found the formation of SRO as another intermediate solution to minimize the lattice distortion induced by the atomic size mismatch, in order to stabilize this metastable system against phase separation. When the Sn composition further increases, though, eventually even SRO won't be enough to fully reconcile the local distortion induced by the atomic size mismatch, and phase separation would occur. Therefore, this finding enriches our understanding of fundamental thermodynamics and phase stability in atomic size mismatched alloys systems by taking SRO into account.

We also developed a better understanding of APT SRO analysis techniques. While APT analysis has been applied to SiGeSn thin films previously,[52] conventional approaches only allow analyzing the atomic neighbors beyond 3NN. The Poisson-KNN method allows us to investigate atomic SRO in 1NN-3NN for the first time in SiGeSn alloys. The observed tendency of Si-Si attraction is highly consistent with the theoretical modeling especially after considering the impact of atomic position perturbation in APT measurements. Relatively stronger Si-Si 1NN preference is observed when Si:Sn ratio becomes smaller, supporting the idea that SRO exists to minimize the distortion (or strain) created by the substitution of Si and Sn in the Ge lattice. The relative comparison of Sn-Sn SRO is also qualitatively consistent with the theoretical predictions for SiGeSn vs. GeSn, as discussed earlier, although the absolute Sn-Sn SRO parameters are less accurate than that of Si-Si. This discrepancy arises because (1) Sn-Sn SRO is more sensitive to atomic position perturbation since 1NN and 3NN are opposite in repulsion vs. preference. The intermixing of 1NN and 3NN due to atomic position perturbation will dramatically compensate 1NN SRO and artificially randomize the alloy; (2) Sn atoms have a stronger tendency to migrate under a large electric field in the APT data collection. Overall, we find that the accuracy of APT SRO analyses depends not only on the nature of SRO for different atomic species, but also the migration of the atomic species under high electric field and thermal perturbation induced by the laser pulses. Close collaborations with theoretical modeling and cross-check with other techniques, such as 4D-STEM [61, 62], would be ideal to better understand and interpret the APT SRO data.

Moreover, the theoretically predicted coexistence of two types of SRO in SiGeSn with higher Si and Sn compositions [39] suggests that the mean value of SRO over a

large area is not enough to reveal the atomic structure in a complex alloy. Instead, local atomic ordering should be characterized by the distribution of the SRO parameter in both real space and SRO parameter space.[42, 68] Thus the 3D SRO map and histogram we obtained from APT data are informative and greatly complementary to the averaged results from EXAFS [51] in SRO analyses.

We also found that modifying CVD precursors can potentially control the SRO in SiGeSn growth process. It is known that surface chemistry and reconstruction on the substrate impact the crystal growth process.[69–72] By using different precursors, kinetics of the surface reactions could lead to different chemical bonding associated with surface reconstruction, and this local ordering could in turn foreshadow the nucleation.[73, 74] Previous studies show that Ti-based precursors can influence the SRO in Ti-doped $NaAlH_4$,[75, 76] and Bi surfactant can dramatically change the atomic ordering in GaAsSb and GaAsN.[77, 78] These studies echo with our discovery that SRO in SiGeSn alloys could be tuned by varying Si precursors, although the impact of precursor is still subtle in our results and the detailed mechanism needs further exploration.

Since Si precursor could impact the SRO of Si, we expect that engineering Sn precursors might also have an impact on the SRO of Sn. Currently, $SnCl_4$ is the dominant CVD precursor for Sn. However, other precursors such as SnD_4 are being studied. We have also investigated SRO in GeSn grown by different Ge precursors. It is found Ge precursor (GeH_4 or Ge_2H_6) seems to have a small impact on Sn-Sn SRO in GeSn, see Supporting Information Fig. S2. We will explore the influence of the Sn CVD precursor on Sn-Sn SRO in GeSn and SiGeSn in future research.

The significance of this work is that it indicates the possibility of controlling SRO in SiGeSn by tuning growth methods, e.g. switching between different precursors in CVD growths. As SRO can significantly impact the bandgap of SiGeSn,[39] lattice-matched hetero-junction with the same composition/lattice constant but different SRO and bandgaps across the interface could potentially be achievable.[43] This could resolve the long-existing materials growth issue brought by lattice mismatch, thus offering a new degree of freedom to achieve high quality lattice-matched SiGeSn hetero-junctions and QWs for optoelectronic applications such as lasers, modulators and photodetectors. Potential transitions from random to SRO alloys and vice versa by swapping neighboring atoms under thermal or electrical pulse excitation may also open a door towards novel phase-change optoelectronic devices on Si based on SRO rather than LRO in existing systems (e.g. amorphous-to-crystalline or random to LRO alloys), which can potentially boost the speed and energy efficiency of the phase transition process. The study of SRO in SiGeSn is the beginning of better understanding the atomic ordering and pathways to its control in advanced Si-based semiconductor alloys that may include all Group IV elements such as quaternary CSiGeSn alloys.

3 Conclusion

In summary, we investigated the SRO in $Si_xGe_{1-x-y}Sn_y$ (x<12%, y<16%) grown by CVD, utilizing advanced APT SRO analysis techniques. Notable Si-Si 1NN preference is observed and its dependence on Si/Sn ratio is consistent with theoretical

modeling. The modeling was achieved through large-scale atomistic simulations using state-of-the-art machine-learning neuroevolution potentials developed specifically for SiGeSn, which provide first-principles accuracy and enable side-by-side experiment-theory comparisons at the same spatial scale. To our knowledge, this is the first APT experimental work revealing 3D SRO mapping and statistical histograms in SiGeSn alloys. It also represents the first observation of notable SRO in dilute semiconductor alloys, revealing a strong impact of atomic size mismatch on SRO. We also reveal the impact of Si precursors on the SRO in SiGeSn, potentially offering an effective and facile approach to control the SRO as a new degree of freedom in band engineering towards high-quality lattice-matched iso-composition SRO hetero-junction and QWs in SiGeSn devices for infrared optoelectronic applications. Furthermore, transitions between SRO and random SiGeSn alloys at the same composition under thermal or electrical excitation may also potentially offer new mechanisms for designing novel phase-change semiconductor materials and devices on Si.

4 Methods

APT conditions: APT conditions for each sample is listed in Table 4. Cameca IVAS software were used to reconstructed APT data.

Table 4 APT conditions

Sample #	Mode	Laser energy (pJ)	Laser wavelength (nm)	Pulse frequency (kHz)	Base temperature (K)
A1	Laser	60	355	125	30
	Laser	20	355	125	30
	Laser	10	355	125	30
	Voltage	0	\	200	50
A2	Laser	50	260	138	30
	Laser	10	355	125	30
	Voltage	0	\	125	30
A3	Laser	50	260	138	30
A4	Laser	50	260	138	30
B1	Laser	10	355	200	50
B2	Laser	10	355	200	50
B3	Laser	20	355	200	60
B4	Laser	20	355	200	50
C1	Laser	50	260	138	60
C2	Laser	20	355	250	30
C3	Laser	20	355	250	30
C4	Laser	20	355	125	30
C5	Laser	20	355	125	30
C6	Laser	20	355	125	30

Poisson-KNN method: The SRO is quantified using Poisson-KNN method developed in reference [60]. True KNN is obtained by a statistically weighted summation of nominal KNN from APT data. The counts of A-B pairs (A, B = Si, Ge, Sn) in the true KNN shell are determined by weighted sums of the A-B pairs in the nominal KNN

shells. The probability of A-B pairs is then calculated and compared with the compositions. This statistical Poisson-KNN method is verified by a rectification approach, which uses a least squares fit to adjust atoms to nearby perfect lattice sites.[60] The robustness of the Poisson-KNN method is also tested using GeSn, as described in reference [65], where the theoretical supercell of $Ge_{0.75}Sn_{0.25}$ with and without SRO can be clearly distinguished even under perturbation of up to 3 Å.

DFT calculations: The SRO structure used to calculate band structure was obtained from DFT-based Monte Carlo sampling (MC/DFT).[39, 40] The simulation cell containing 64 atoms is created by replicating a conventional diamond cubic cell twice along each dimension. DFT calculations were performed using the Vienna ab initio simulation package (VASP) [79] with the projector augmented wave method,[80–82], a 2×2×2 Monkhorst-Pack k-points grid [83], a plane-wave cutoff energy of 300 eV, and local density approximation (LDA) [84] as the exchange-correlation functional. LDA has been demonstrated to yield the best agreement with experiment results for structure optimization of pure Ge and Sn.[85–88] The conjugate-gradient algorithm is employed to perform full structural relaxation, including cell volume, cell shape, and atomic positions, with convergence criteria of 10^{-5} eV for electronic relaxations and 10^{-4} eV for ionic relaxations.

Band structure calculations: For band structure calculations, we utilized the modified Becke-Johnson (mBJ) exchange potential,[86] implemented in the VASP [79] code, with the c-mBJ parameter of 1.2, which has been shown to predict accurate band gaps for Si, Ge, and α-Sn, demonstrating good agreement with experimental data and superior computational efficiency compared to hybrid functionals or GW methods.[43, 86–88] Spectral weight approach [89, 90] was used to unfold the band structures back into the first Brillouin Zone of the diamond cubic structure. The unfolding was performed using the fold2bloch code [90] on 128-atom supercells, transformed from the 64-atom SRO and special quasi-random structure (SQS) [91] supercells. The transformation matrix is [[0, 1, 1], [1, 0, 1], [1, 1, 0]]. Spin-orbit coupling is included in the band structure calculations, as it is crucial for accurately reproducing the band structures of Ge and α-Sn.[40, 43, 87, 88]

Neuroevolution potential for large-scale atomistic simulations: We trained neuroevolution potentials (NEPs) for SiGeSn alloys, extending our previously developed NEPs for GeSn alloys [42], based on NEP4 neural network architecture for multi-component alloy systems [92]. The training and test datasets were constructed based on DFT calculations [39, 40]. The training dataset includes MC/DFT trajectories of $Si_{0.25}Ge_{0.5}Sn_{0.25}$ (21 759 structures) and $Si_{0.125}Ge_{0.625}Sn_{0.25}$ under 1% of tensile strain (17 309 structures) and 1% of compressive strain (13 025 structures), as well as 137 representative GeSn alloy structures selected via farthest point sampling (FPS) of a comprehensive GeSn MC/DFT dataset that comprises a broad range of GeSn compositions[40, 42]. The training dataset contains 52 230 structures and 3 342 720 atoms in total. The test dataset was constructed from an MC/DFT trajectory of a different composition, $Si_{0.0625}Ge_{0.6875}Sn_{0.25}$, and includes 7153 structures and 457 792 atoms. We used GPUMD package [93, 94] v3.6 to train the NEP4 model for SiGeSn alloys. The detailed input hyperparameters are provided in supporting information. The training accuracy of our NEP4 model based on the entire training dataset reaches

an excellent level, achieving a root-mean-square error (RMSE) of 0.3 meV/atom for energy and 14.1 meV/Å for force, respectively. The predictive (test) accuracy is also outstanding, achieving a RMSE of 0.34 meV/atom for energy and 11.6 meV/Å for force, respectively. By applying FPS to the entire training dataset, we obtained a reduced FPS training dataset, based on which we trained another NEP4 model that maintains a similar level of predictive (test) accuracy (RMSE of 0.27 meV/atom for energy and 12.4 meV/Å for force on the same test dataset) while reducing computational cost. We further validated our developed NEP using MC/DFT trajectories of a dilute composition $Si_{0.0625}Ge_{0.875}Sn_{0.0625}$, containing 191 547 structures and 12 259 008 atoms. Our developed NEPs enable large-scale atomistic simulations leveraging GPU acceleration as implemented in GPUMD package [93, 94], surpassing the spatiotemporal constraints of DFT while maintaining DFT-level accuracy. Large-scale ($10.2\times10.2\times10.2$ nm^3) SiGeSn supercells with SRO were generated using MC sampling with the highly accurate and efficient NEP we developed herein for SiGeSn alloys, based on the FPS training dataset, which demonstrates outstanding energy accuracy and comparably excellent force accuracy (with RMSE of 0.2 meV/atom for relative energy and 14.3 meV/Å for force on the validation dataset).

Supplementary information. Poisson-KNN method on theoretically simulated supercell data. Short-range order in GeSn grown by different Ge precursors. Input hyperparameters for training the machine-learning neuronevolution potentials for SiGeSn alloys.

Acknowledgments. The statistical method of analyzing SRO from the APT data has been developed under the support of the Air Force Office of Scientific Research under the award number FA9550-19-1-0341 managed by Dr. Gernot Pomrenke and Dr. Wooddy Miller. The APT tip preparation and data collection of the SiGeSn samples provided by University of Arkansas have been supported as part of μ-ATOMS, an Energy Frontier Research Center funded by the U.S. Department of Energy (DOE), Office of Science, Basic Energy Sciences (BES), under the award DE-SC0023412. Part of the APT research was supported by the Center for Nanophase Materials Sciences (CNMS), which is a US Department of Energy, Office of Science User Facility at Oak Ridge National Laboratory. The authors would like to thank James Burns for assistance in performing APT sample preparation and running the APT experiments. The authors would like to thank Dr. Jonathan D. Poplawsky for reconstructing the samples run at the CNMS.

Declarations

- Funding
- Conflict of interest/Competing interests
  The authors declare no conflict of interest.
- Ethics approval
- Consent to participate
- Consent for publication
- Availability of data and materials

The data that support the findings of this study are available from the corresponding author upon reasonable request.

- Code availability
  The code are available from the corresponding author upon reasonable request.
- Authors' contributions
  J.L. conceived and supervised this project. S.L. implemented the program and analyzed the APT data with A.C. and X.W. J.B., I.B., C.C., A.A. and D.J. conducted APT data acquisition and reconstruction. S.C., X.J. and T.L. developed first-principles machine-learning neuroevolution potentials for SiGeSn alloys, generated theoretical SiGeSn supercell data and calculated the band structures. L.V. and A.M. provided STEM and EDS data. H.Z. and Y.Z. contributed to composition characterization. O.C., D.B. and S.Y. managed materials growth and provided the SiGeSn samples.

References

[1] Fan, C.C.: What mencius's mother sought. The New York Times (2011)

[2] Chen, X., Wang, Q., Cheng, Z., Zhu, M., Zhou, H., Jiang, P., Zhou, L., Xue, Q., Yuan, F., Zhu, J., *et al.*: Direct observation of chemical short-range order in a medium-entropy alloy. Nature **592**(7856), 712–716 (2021)

[3] Ding, Q., Zhang, Y., Chen, X., Fu, X., Chen, D., Chen, S., Gu, L., Wei, F., Bei, H., Gao, Y., *et al.*: Tuning element distribution, structure and properties by composition in high-entropy alloys. Nature **574**(7777), 223–227 (2019)

[4] Zhang, R., Zhao, S., Ding, J., Chong, Y., Jia, T., Ophus, C., Asta, M., Ritchie, R.O., Minor, A.M.: Short-range order and its impact on the crconi medium-entropy alloy. Nature **581**(7808), 283–287 (2020)

[5] Lei, Z., Liu, X., Wu, Y., Wang, H., Jiang, S., Wang, S., Hui, X., Wu, Y., Gault, B., Kontis, P., *et al.*: Enhanced strength and ductility in a high-entropy alloy via ordered oxygen complexes. Nature **563**(7732), 546–550 (2018)

[6] Ferrari, A., Körmann, F., Asta, M., Neugebauer, J.: Simulating short-range order in compositionally complex materials. Nature Computational Science **3**(3), 221–229 (2023)

[7] Li, Y., Wei, Y., Wang, Z., Liu, X., Colnaghi, T., Han, L., Rao, Z., Zhou, X., Huber, L., Dsouza, R., *et al.*: Quantitative three-dimensional imaging of chemical short-range order via machine learning enhanced atom probe tomography. Nature Communications **14**(1), 7410 (2023)

[8] He, M., Davids, W.J., Breen, A.J., Ringer, S.P.: Quantifying short-range order using atom probe tomography. Nature Materials, 1–8 (2024)

[9] George, E.P., Raabe, D., Ritchie, R.O.: High-entropy alloys. Nature reviews

materials **4**(8), 515–534 (2019)

[10] Murty, B.S., Yeh, J.-W., Ranganathan, S., Bhattacharjee, P.P.: High-entropy Alloys. Elsevier, Netherlands (2019)

[11] Svoboda, J., Holec, D., Popov, M., Zickler, G., Fischer, F.-D.: Modelling of short-range ordering kinetics in dilute multicomponent substitutional solid solutions. Philosophical magazine **100**(15), 1942–1961 (2020)

[12] Maurer, M., C. Cadeville, M.: Short range order in dilute fe sbt alloys (t= ni, co, cr) investigated by zero field nmr at 121sb and 59co nuclei. Journal of the Physical Society of Japan **50**(2), 445–450 (1981)

[13] Veillet, P., Campbell, I., *et al.*: Short-range order in dilute iron alloys. Journal of Physics F: Metal Physics **5**(11), 203 (1975)

[14] Gerold, V., Karnthaler, H.: On the origin of planar slip in fcc alloys. Acta Metallurgica **37**(8), 2177–2183 (1989)

[15] Zhang, R., Zhao, S., Ophus, C., Deng, Y., Vachhani, S.J., Ozdol, B., Traylor, R., Bustillo, K.C., Morris Jr, J., Chrzan, D.C., *et al.*: Direct imaging of short-range order and its impact on deformation in ti-6al. Science advances **5**(12), 2799 (2019)

[16] Mascarenhas, A.: Spontaneous Ordering in Semiconductor Alloys. Springer, New York (2002)

[17] Ciatto, G., d'Acapito, F., Grenouillet, L., Mariette, H., De Salvador, D., Bisognin, G., Carboni, R., Floreano, L., Gotter, R., Mobilio, S., *et al.*: Quantitative determination of short-range ordering in InxGa1-xAs1-yNy. Physical Review B **68**(16), 161201 (2003)

[18] Tran, H., Pham, T., Margetis, J., Zhou, Y., Dou, W., Grant, P.C., Grant, J.M., Al-Kabi, S., Sun, G., Soref, R.A., *et al.*: Si-based gesn photodetectors toward mid-infrared imaging applications. ACS Photonics **6**(11), 2807–2815 (2019)

[19] Atalla, M.R., Assali, S., Koelling, S., Attiaoui, A., Moutanabbir, O.: High-bandwidth extended-swir gesn photodetectors on silicon achieving ultrafast broadband spectroscopic response. ACS Photonics **9**(4), 1425–1433 (2022)

[20] Wang, L., Zhang, Y., Wu, Y., Liu, T., Miao, Y., Meng, L., Jiang, Z., Hu, H.: Effects of annealing on the behavior of sn in gesn alloy and gesn-based photodetectors. IEEE Transactions on Electron Devices **67**(8), 3229–3234 (2020)

[21] Chen, Q., Zhou, H., Xu, S., Huang, Y.-C., Wu, S., Lee, K.H., Gong, X., Tan, C.S.: A route toward high-detectivity and low-cost short-wave infrared photodetection: Gesn/ge multiple-quantum-well photodetectors with a dielectric nanohole array metasurface. ACS nano **17**(13), 12151–12159 (2023)

[22] Chang, C., Cheng, H.-H., Sevison, G.A., Hendrickson, J.R., Li, Z., Agha, I., Mathews, J., Soref, R.A., Sun, G.: Power-dependent investigation of photo-response from gesn-based pin photodetector operating at high power density. Materials **15**(3), 989 (2022)

[23] Zhao, H., Lin, G., Han, C., Hickey, R., Zhama, T., Cui, P., Deroy, T., Feng, X., Ni, C., Zeng, Y.: Improving the short-wave infrared response of strained gesn/ge multiple quantum wells by rapid thermal annealing. Vacuum **210**, 111868 (2023)

[24] Liu, C.-H., Bansal, R., Wu, C.-W., Jheng, Y.-T., Chang, G.-E.: Gesn waveguide photodetectors with vertical p–i–n heterostructure for integrated photonics in the 2 μm wavelength band. Advanced Photonics Research **3**(7), 2100330 (2022)

[25] Zhou, Y., Miao, Y., Ojo, S., Tran, H., Abernathy, G., Grant, J.M., Amoah, S., Salamo, G., Du, W., Liu, J., *et al.*: Electrically injected gesn lasers on si operating up to 100 k. Optica **7**(8), 924–928 (2020)

[26] Zhou, Y., Ojo, S., Wu, C.-W., Miao, Y., Tran, H., Grant, J.M., Abernathy, G., Amoah, S., Bass, J., Salamo, G., *et al.*: Electrically injected gesn lasers with peak wavelength up to 2.7 μm. Photonics Research **10**(1), 222–229 (2022)

[27] Marzban, B., Seidel, L., Liu, T., Wu, K., Kiyek, V., Zoellner, M.H., Ikonic, Z., Schulze, J., Grützmacher, D., Capellini, G., *et al.*: Strain engineered electrically pumped sigesn microring lasers on si. ACS Photonics **10**(1), 217–224 (2022)

[28] Liu, T., Seidel, L., Marzban, B., Oehme, M., Witzens, J., Capellini, G., Grützmacher, D., Buca, D.: Electrically pumped gesn/sigesn micro-rings lasers on si with minimum threshold current of 40 ma. In: 2023 IEEE Silicon Photonics Conference (SiPhotonics), pp. 1–2 (2023). IEEE

[29] Driesch, N., Stange, D., Rainko, D., Povstugar, I., Zaumseil, P., Capellini, G., Schröder, T., Denneulin, T., Ikonic, Z., Hartmann, J.-M., *et al.*: Advanced gesn/sigesn group iv heterostructure lasers. Advanced science **5**(6), 1700955 (2018)

[30] Margetis, J., Zhou, Y., Dou, W., Grant, P.C., Alharthi, B., Du, W., Wadsworth, A., Guo, Q., Tran, H., Ojo, S., *et al.*: All group-iv sigesn/gesn/sigesn qw laser on si operating up to 90 k. Applied Physics Letters **113**(22), 221104 (2018)

[31] Stange, D., Driesch, N., Zabel, T., Armand-Pilon, F., Rainko, D., Marzban, B., Zaumseil, P., Hartmann, J.-M., Ikonic, Z., Capellini, G., *et al.*: Gesn/sigesn heterostructure and multi quantum well lasers. ACS photonics **5**(11), 4628–4636 (2018)

[32] Marzban, B., Stange, D., Rainko, D., Ikonic, Z., Buca, D., Witzens, J.: Modeling of a sigesn quantum well laser. Photonics Research **9**(7), 1234–1254 (2021)

[33] Abernathy, G., Ojo, S., Grant, J.M., Zhou, Y., Du, W., Kuchuk, A., Li, B., Yu, S.-Q.: Study of critical optical confinement factor for gesn-based multiple quantum well lasers. Applied Physics Letters **121**(17) (2022)

[34] Olorunsola, O., Said, A., Ojo, S., Stanchu, H., Abernathy, G., Amoah, S., Saha, S., Wangila, E., Grant, J., Acharya, S., *et al.*: Study of sigesn-based multiple quantum well laser for photonics integrated circuits. In: Society of Photo-Optical Instrumentation Engineers (SPIE) Conference Series, vol. 12426, p. 124260 (2023)

[35] Moutanabbir, O., Assali, S., Gong, X., O'Reilly, E., Broderick, C., Marzban, B., Witzens, J., Du, W., Yu, S.-Q., Chelnokov, A., et al.: Monolithic infrared silicon photonics: The rise of (si) gesn semiconductors. Applied Physics Letters **118**(11) (2021)

[36] Wang, X., Cuervo Covian, A., Je, L., Fu, S., Li, H., Piao, J., Liu, J.: Gesn on insulators (gesnoi) toward mid-infrared integrated photonics. Frontiers in Physics **7**, 134 (2019)

[37] Olorunsola, O., Said, A., Ojo, S., Stanchu, H., Abernathy, G., Amoah, S., Saha, S., Wangila, E., Grant, J., Acharya, S., et al.: Sigesn quantum well for photonics integrated circuits on si photonics platform: a review. Journal of Physics D: Applied Physics (2022)

[38] Sun, G., Soref, R., Cheng, H.: Design of a si-based lattice-matched room-temperature gesn/gesisn multi-quantum-well mid-infrared laser diode. Optics express **18**(19), 19957–19965 (2010)

[39] Jin, X., Chen, S., Li, T.: Coexistence of two types of short-range order in Si–Ge–Sn medium-entropy alloys. Communications Materials **3**(1), 66 (2022)

[40] Cao, B., Chen, S., Jin, X., Liu, J., Li, T.: Short-range order in GeSn alloy. ACS Applied Materials & Interfaces **12**(51), 57245–57253 (2020)

[41] Jin, X., Chen, S., Li, T.: Short-range order in SiSn alloy enriched by second-nearest-neighbor repulsion. Physical Review Materials **5**(10), 104606 (2021)

[42] Chen, S., Jin, X., Zhao, W., Li, T.: Intricate short-range order in GeSn alloys revealed by atomistic simulations with highly accurate and efficient machine-learning potentials. Physical Review Materials **8**(4), 043805 (2024)

[43] Jin, X., Chen, S., Li, T.: Enabling type I lattice-matched heterostructures in sigesn alloys through engineering composition and short-range order: A first-principles perspective. IEEE Journal of Selected Topics in Quantum Electronics (2024)

[44] Chen, S., Li, T.: Impacts of short-range order on thermal conductivity of Si-Ge-Sn alloys. In: APS March Meeting Abstracts, vol. 2023, pp. 61–008 (2023)

[45] Peng, Y., Miao, L., Liu, C., Song, H., Kurosawa, M., Nakatsuka, O., Back, S.Y., Rhyee, J.S., Murata, M., Tanemura, S., *et al.*: Constructed ge quantum dots and sn precipitate sigesn hybrid film with high thermoelectric performance at low temperature region. Advanced Energy Materials **12**(2), 2103191 (2022)

[46] Spirito, D., Driesch, N., Manganelli, C.L., Zoellner, M.H., Corley-Wiciak, A.A., Ikonic, Z., Stoica, T., Grutzmacher, D., Buca, D., Capellini, G.: Thermoelectric efficiency of epitaxial gesn alloys for integrated si-based applications: assessing the lattice thermal conductivity by raman thermometry. ACS Applied Energy Materials **4**(7), 7385–7392 (2021)

[47] Liu, D., Wang, Q., Wang, J., Chen, X., Jiang, P., Yuan, F., Cheng, Z., Ma, E., Wu, X.: Chemical short-range order in fe50mn30co10cr10 high-entropy alloy. Materials Today Nano **16**, 100139 (2021)

[48] Zhou, L., Wang, Q., Wang, J., Chen, X., Jiang, P., Zhou, H., Yuan, F., Wu, X., Cheng, Z., Ma, E.: Atomic-scale evidence of chemical short-range order in crconi medium-entropy alloy. Acta Materialia **224**, 117490 (2022)

[49] Walsh, F., Zhang, M., Ritchie, R.O., Minor, A.M., Asta, M.: Extra electron reflections in concentrated alloys do not necessitate short-range order. nature materials **22**(8), 926–929 (2023)

[50] Walsh, F., Zhang, M., Ritchie, R.O., Asta, M., Minor, A.M.: Multiple origins of extra electron diffractions in fcc metals. Science Advances **10**(31), 9673 (2024) https://doi.org/10.1126/sciadv.adn9673

[51] Shimura, Y., Asano, T., Yamaha, T., Fukuda, M., Takeuchi, W., Nakatsuka, O., Zaima, S.: Exafs study of local structure contributing to sn stability in siyge1-y-zsnz. Materials Science in Semiconductor Processing **70**, 133–138 (2017)

[52] Mukherjee, S., Kodali, N., Isheim, D., Wirths, S., Hartmann, J., Buca, D., Seidman, D.N., Moutanabbir, O.: Short-range atomic ordering in nonequilibrium silicon-germanium-tin semiconductors. Physical Review B **95**(16), 161402 (2017)

[53] Ceguerra, A.V., Powles, R.C., Moody, M.P., Ringer, S.P.: Quantitative description of atomic architecture in solid solutions: a generalized theory for multicomponent short-range order. Physical Review B **82**(13), 132201 (2010)

[54] Zhou, J., Odqvist, J., Thuvander, M., Hedström, P.: Quantitative evaluation of spinodal decomposition in fe-cr by atom probe tomography and radial distribution function analysis. Microscopy and Microanalysis **19**(3), 665–675 (2013)

[55] Gault, B., Moody, M.P., De Geuser, F., La Fontaine, A., Stephenson, L.T., Haley, D., Ringer, S.P.: Spatial resolution in atom probe tomography. Microscopy and Microanalysis **16**(1), 99–110 (2010)

[56] Geiser, B.P., Kelly, T.F., Larson, D.J., Schneir, J., Roberts, J.P.: Spatial distribution maps for atom probe tomography. Microscopy and Microanalysis **13**(6), 437–447 (2007)

[57] Philippe, T., Gruber, M., Vurpillot, F., Blavette, D.: Clustering and local magnification effects in atom probe tomography: a statistical approach. Microscopy and Microanalysis **16**(5), 643–648 (2010)

[58] Waugh, A., Boyes, E., Southon, M.: Investigations of field evaporation with a field-desorption microscope. Surface Science **61**(1), 109–142 (1976)

[59] Birdseye, P., Smith, D., Smith, G.: Analogue investigations of electric field distribution and ion trajectories in the field ion microscope. Journal of Physics D: Applied Physics **7**(12), 1642 (1974)

[60] Liu, S., Covian, A.C., Wang, X., Cline, C.T., Akey, A., Dong, W., Yu, S.-Q., Liu, J.: 3d nanoscale mapping of short-range order in gesn alloys. Small Methods **6**(5), 2200029 (2022)

[61] Vogl, L.M., Schweizer, P., Chen, S., Jin, X., Yu, S.-Q., Byrne, D.O., Allen, F.I., Liu, J., Li, T., Minor, A.M.: Exploring Short-Range Ordering in Semiconducting Materials. Microscopy and Microanalysis **30**(Supplement_1), 044–565 (2024)

[62] Vogl, L.M., Schweizer, P., Chen, S., Jin, X., Yu, S.-Q., Byrne, D.O., Allen, F.I., Liu, J., Li, T., Minor, A.M.: Identification of SRO in semiconducting materials. To be submitted.

[63] Zhong, X., Chen, L., Medgyes, B., Zhang, Z., Gao, S., Jakab, L.: Electrochemical migration of sn and sn solder alloys: a review. RSC advances **7**(45), 28186–28206 (2017)

[64] Liang, S., Ke, C., Ma, W., Zhou, M., Zhang, X.: Numerical simulations of migration and coalescence behavior of microvoids driven by diffusion and electric field in solder interconnects. Microelectronics Reliability **71**, 71–81 (2017)

[65] Liu, S., Liang, Y., Zhao, H., Eldose, N.M., Bae, J.-H., Concepcion, O., Jin, X., Chen, S., Bikmukhametov, I., Akey, A., Cline, C.T., Covian, A.C., Wang, X., Li, T., Zeng, Y., Buca, D., Yu, S.-Q., Salamo, G.J., Zhang, S., Liu, J.: Comparison of short-range order in GeSn grown by molecular beam epitaxy and chemical vapor deposition (2024) arXiv:2407.02767 [cond-mat.mtrl-sci]

[66] Gault, B., Moody, M.P., Cairney, J.M., Ringer, S.P.: Atom Probe Microscopy vol. 160. Springer, New York (2012)

[67] Wirths, S., Buca, D., Mantl, S.: Si–ge–sn alloys: From growth to applications. Progress in crystal growth and characterization of materials **62**(1), 1–39 (2016)

[68] Jin, X., Chen, S., Lemkan, C., Li, T.: Role of local atomic short-range order distribution in alloys: Why it matters in Si-Ge-Sn alloys. Physical Review Materials **7**(11), 111601 (2023)

[69] Batyrev, I.G., Norman, A.G., Zhang, S., Wei, S.-H.: Growth model for atomic ordering: The case for quadruple-period ordering in gaassb alloys. Physical review letters **90**(2), 026102 (2003)

[70] Bi, Y., Cabriolu, R., Li, T.: Heterogeneous ice nucleation controlled by the coupling of surface crystallinity and surface hydrophilicity. The Journal of Physical Chemistry C **120**(3), 1507–1514 (2016)

[71] Bi, Y., Cao, B., Li, T.: Enhanced heterogeneous ice nucleation by special surface geometry. Nature communications **8**(1), 15372 (2017)

[72] Liu, S., Li, S., Gardener, J.A., Akey, A., Gao, X., Wang, X., Liu, J.: Phase-pure α-sn quantum material on si seeded by a 2 nm-thick ge layer. Small Methods, 2400550 (2024)

[73] Lu, Y., Lu, X., Qin, Z., Shen, J.: Experimental evidence for ordered precursor foreshadowing crystal nucleation in colloidal system. Solid State Communications **217**, 13–16 (2015)

[74] Egusa, D., Kawaguchi, K., Abe, E.: Direct observations of precursor short-range order clusters of solute atoms in a lpso-forming mg-zn-gd ternary alloy. Frontiers in Materials **6**, 266 (2019)

[75] Léon, A., Rothe, J., Fichtner, M.: Variation and influence of the local structure around ti in naalh4 doped with a ti-based precursor. The Journal of Physical Chemistry C **111**(44), 16664–16669 (2007)

[76] Léon, A., Kircher, O., Fichtner, M., Rothe, J., Schild, D.: Evolution of the local structure around ti atoms in naalh4 doped with ticl3 or ti13·6thf by ball milling using x-ray absorption and x-ray photoelectron spectroscopy. The Journal of Physical Chemistry B **110**(3), 1192–1200 (2006)

[77] Jiang, W., Liu, J., So, M., Rao, T., Thewalt, M., Kavanagh, K., Watkins, S.: Effect of bi surfactant on atomic ordering of gaassb. Applied physics letters **85**(23), 5589–5591 (2004)

[78] Occena, J., Jen, T., Lu, H., Carter, B., Jimson, T., Norman, A., Goldman, R.: Surfactant-induced chemical ordering of gaasn: Bi. Applied Physics Letters **113**(21), 211602 (2018)

[79] Kresse, G., Hafner, J.: Ab initio molecular dynamics for liquid metals. Physical review B **47**(1), 558 (1993)

[80] Kresse, G., Joubert, D.: From ultrasoft pseudopotentials to the projector augmented-wave method. Physical review b **59**(3), 1758 (1999)

[81] Kresse, G., Furthmüller, J.: Efficiency of ab-initio total energy calculations for metals and semiconductors using a plane-wave basis set. Computational materials science **6**(1), 15–50 (1996)

[82] Kresse, G., Furthmüller, J.: Efficient iterative schemes for ab initio total-energy calculations using a plane-wave basis set. Physical review B **54**(16), 11169 (1996)

[83] Monkhorst, H.J., Pack, J.D.: Special points for brillouin-zone integrations. Physical review B **13**(12), 5188 (1976)

[84] Ceperley, D.M., Alder, B.J.: Ground state of the electron gas by a stochastic method. Physical review letters **45**(7), 566 (1980)

[85] Haas, P., Tran, F., Blaha, P.: Calculation of the lattice constant of solids with semilocal functionals. Physical Review B—Condensed Matter and Materials Physics **79**(8), 085104 (2009)

[86] Tran, F., Blaha, P.: Accurate band gaps of semiconductors and insulators with a semilocal exchange-correlation potential. Physical review letters **102**(22), 226401 (2009)

[87] Eckhardt, C., Hummer, K., Kresse, G.: Indirect-to-direct gap transition in strained and unstrained sn x ge 1- x alloys. Physical Review B **89**(16), 165201 (2014)

[88] Polak, M., Scharoch, P., Kudrawiec, R.: The electronic band structure of ge1-xsnx in the full composition range: indirect, direct, and inverted gaps regimes, band offsets, and the burstein–moss effect. Journal of Physics D: Applied Physics **50**(19), 195103 (2017)

[89] Popescu, V., Zunger, A.: Effective band structure of random alloys. Physical review letters **104**(23), 236403 (2010)

[90] Rubel, O., Bokhanchuk, A., Ahmed, S., Assmann, E.: Unfolding the band structure of disordered solids: From bound states to high-mobility kane fermions. Physical Review B **90**(11), 115202 (2014)

[91] Zunger, A., Wei, S.-H., Ferreira, L., Bernard, J.E.: Special quasirandom structures. Physical review letters **65**(3), 353 (1990)

[92] Song, K., Zhao, R., Liu, J., Wang, Y., Lindgren, E., Wang, Y., Chen, S., Xu, K., Liang, T., Ying, P., Xu, N., Zhao, Z., Shi, J., Wang, J., Lyu, S., Zeng, Z., Liang, S., Dong, H., Sun, L., Chen, Y., Zhang, Z., Guo, W., Qian, P., Sun, J., Erhart, P., Ala-Nissila, T., Su, Y., Fan, Z.: General-purpose machine-learned potential

for 16 elemental metals and their alloys (2023) https://doi.org/10.48550/arXiv.2311.04732 arXiv:2311.04732 [cond-mat.mtrl-sci]

[93] Fan, Z., Chen, W., Vierimaa, V., Harju, A.: Efficient molecular dynamics simulations with many-body potentials on graphics processing units. Computer Physics Communications **218**, 10–16 (2017) https://doi.org/10.1016/j.cpc.2017.05.003

[94] Fan, Z., Wang, Y., Ying, P., Song, K., Wang, J., Wang, Y., Zeng, Z., Xu, K., Lindgren, E., Rahm, J.M., Gabourie, A.J., Liu, J., Dong, H., Wu, J., Chen, Y., Zhong, Z., Sun, J., Erhart, P., Su, Y., Ala-Nissila, T.: GPUMD: A package for constructing accurate machine-learned potentials and performing highly efficient atomistic simulations. The Journal of Chemical Physics **157**(11), 114801 (2022) https://doi.org/10.1063/5.0106617

Supplementary Files

This is a list of supplementary files associated with this preprint. Click to download.

- SiGeSnSROSuppInfo.pdf